Supplemental Data

Supplemental Information

Supplemental Information includes supplementary tables, figures, discussion, text describing additional experimental procedures, and references.

Supplemental Tables

SI Beta Events											
Subject	**1**	**2**	**3**	**4**	**5**	**6**	**7**	**8**	**9**	**10**	**Across Subject (sign-test)**
number of beta events	50	50	50	50	50	50	50	50	50	50	
peak beta frequency	20	18	18	20	21	21	22	18	19	19	
period (ms)	50.0	55.56	55.56	50.0	47.62	47.62	45.45	55.56	52.63	52.63	
number of periods in a beta epoch	3.88	3.07	3.07	3.21	3.63	3.21	3.37	4.13	3.19	2.95	
PK3 duration (mean +/- SD)	53.1 +/- 11.5	56.3 +/- 10.1	63.8 +/- 10.0	55.2 +/- 10.0	59.8 +/- 8.26	50.6 +/- 9.28	48.6 +/- 6.94	63.8 +/- 10.3	55.3 +/- 9.18	53.1 +/- 5.88	
PK3 - PK2 and PK4 +	yes	yes	yes	yes	yes	yes	yes	yes	yes	yes	*p=0.00097*
magnitude of PK3 compared to PK1 & PK5	*0.0047*	*1.5e-9*	*2.9e-18*	*7.0e-6*	*1.2e-43*	*4.4e-6*	*1.1e-13*	*1.3e-20*	*1.2e-10*	*3.4e-12*	*p=0.00097*
magnitude of PK3 compared to PK2 & PK4	0.014	*6.7e-31*	*4.3e-7*	*7.11e-5*	*8.3e-19*	*3.3e-5*	*1.5e-6*	*1.8e-14*	*1.1e-10*	*1.8e-7*	*p=0.0097*
slope PK1-PK2 compared to PK2-PK3	0.074	0.012	*0.00055*	*0.0066*	*6.3e-22*	*0.0033*	*4.0e-7*	*1.6e-8*	*0.00019*	*1.1e-5*	*p=0.0439*
slope PK3-PK4 compared to PK4-PK5	0.016	*3.7e-6*	*0.0050*	*0.0056*	*3.0e-15*	*0.0070*	*5.14e-5*	*3.1e-6*	*0.00047*	*1.8e-5*	*p=0.0097*

Table S1: Statistical Analysis of Beta Event Waveform Features in Human SI Signals Shown in Figure 1. Table depicts number of unfiltered high-power beta events analyzed in each of 10 subjects, the corresponding beta frequency and period, the average number of periods in an event using a 98% power threshold determined from an empirical distribution of all beta activity, the duration of the PK3 peak (time from PK2-PK4), evaluation of polarity of peak events, and p-values using one-way ANOVA for within subject peak amplitude comparisons (symmetric waveform) (see Experimental Procedures section "Common Procedures to Identify, Align, and Quantify Beta Event Waveforms For All Data Sets"). The peak beta frequency for each subject was chosen as the frequency with the maximum power in the beta band pooled over all data. The fifty highest power beta events at that fixed frequency (determined from peaks in wavelet spectral power) were used for subsequent analysis and were such that PK3 duration varied for each event. These features are consistent with the middle of the beta event waveform having an inverted Ricker-wavelet shape within and across subjects (Figure 1). Significance level $p<0.005$ (Bonferroni correction for multiple comparisons across 10 subjects $p = 0.05/10$); trend values $p<0.008$). Across subject sign-test ($p<0.05$). Significant values are italicized.

IFC Beta Events										
Subject	**1**	**2**	**3**	**4**	**5**	**6**	**7**	**8**	**9**	**Across Subject (sign-test)**
number of beta events	50	50	50	50	50	50	50	50	50	
peak beta frequency	27	27	25	25	20	27	21	20	25	
period (ms)	37.04	37.04	40.0	40.0	50.0	37.04	47.62	50.0	40.0	
number of periods in a beta epoch	3.93	2.95	2.89	3.20	2.75	3.71	2.73	3.00	3.21	
PK3 duration (mean +/- SD)	40.3 +/- 6.51	42.3 +/- 9.32	44.6 +/- 10.7	47.2 +/- 9.78	49.1 +/- 10.9	44.3 +/- 10.4	50.3+/- 8.21	50.9+/- 7.33	46.2 +/- 8.56	
PK3 - PK2 and PK4 +	yes	yes	yes	yes	yes	yes	yes	yes	yes	*p=0.002*
magnitude of PK3 compared to PK1 & PK5	*0.0058*	*5.8e-7*	*1.8e-8*	0.033	*0.0067*	*1.2e-9*	*0.00093*	*0.00026*	*1.5e-8*	*p=0.002*
magnitude of PK3 compared to PK2 & PK4	0.18	0.14	*0.009*	0.046	0.13	*0.0017*	0.31	0.66	0.032	p=0.98
slope PK1-PK2 compared to PK2-PK3	*0.0028*	*0.0001*	*5.9e-7*	0.41	*0.00013*	*1.4e-5*	0.047	0.022	*0.00013*	p=0.2539
slope PK3-PK4 compared to PK4-PK5	*0.0063*	*9.7e-6*	*0.0018*	*0.0063*	*0.0080*	*6.1e-6*	*0.0090*	*0.00039*	*0.00064*	*p=0.002*

Table S2 Statistical Analysis of Beta Event Waveform Features in Human IFC Signals Shown in Figure 1. Same as for SI data in Table S1. Significance level p<0.0056 (Bonferroni correction for multiple comparisons across 9 subjects p = 0.05/9); trend values p<0.09). Across subject sign-test (p<0.05). Significant values are italicized.

	Human SI Signal	**Human IFC Signal**	**Model Non-Rhythmic Drive Proximal (SD=20ms) Distal (SD=15ms)**	**Model 10Hz Proximal (SD=20ms) 10Hz Distal (SD=15ms)**
Number of beta events	500 (50 per subject)	450 (50 per subject)	50	200 (50 per distal standard deviation)
Duration PK1-PK2	p = 0.00921	*p = 0.0012*	*p = 0.306*	p = 0.822
PK3 duration	*p = 1.79e-14*	*p = 3.88e-13*	*p = 5.85e-9*	*p = 0.014*
Duration PK4-PK5	p = 0.00237	*p = 1.92e-8*	*p = 0.028*	p = 0.129

Table S3: Linear Regression Analysis Comparing Period of each Beta Event with the Time Between Peak Activities in the Event Waveform in Human and Model Data. Table depicts p-values of Pearson's correlation coefficient. The duration of the largest amplitude PK3 peak (duration PK2-PK4) is more highly correlated with the beta period than the time to neighboring peak activities in the human data from each area and in our model (as in Figure 4B and 5B) (see Experimental Procedures section "Common Procedures to Identify, Align, and Quantify Beta Event Waveforms For All Data Sets: Correlation Between Beta Period and Peaks). For this analysis, the highest power beta event in 50 1-second spectrograms was determined individually and correlated with the corresponding peak durations. As such, each event had a potentially different frequency unlike the analysis in Tables S1 and S2.

Model Condition	**Non-rhythmic drive**	**Rhythmic drive**	**Rhythmic drive**	**Rhythmic drive**	**Rhythmic drive**	**Rhythmic drive**	**Rhythmic drive**
prox. drive (frequency, SD)	**-, 20**	**10, 20**	**10, 20**	**10, 20**	**10, 20**	**-, -**	**10, 20**
distal drive (frequency, SD)	**-, 15**	**10, 20**	**10, 15**	**10, 10**	**10, 5**	**20, 10**	**20, 10**
number of beta events	50	50	50	50	50	50	50
peak beta frequency	18	18	20	20	20	20	20
period (ms)	55.56	55.56	50	50	50	50	50
PK3 duration (mean +/- SD)	53.2+/- 10.6	59.7 +/- 10.9	52.2 +/- 9.55	50.1 +/- 8.78	44.5 +/- 7.94	49.1 +/- 5.60	47.5 +/- 8.17
PK3 - PK2 and PK4 +	yes	yes	yes	yes	yes	no	yes
Magnitude of PK3 compared to PK1 & PK5	*6.6e-73*	*7.2e-6*	*1.3e-24*	*3.0e-50*	*1.2e-84*	*0.0083*	0.58
Magnitude of PK3 compared to PK2 & PK4	*5.6e-30*	*3.9e-12*	*6.9e-12*	*0.0065*	*0.0097*	N/A	*0.0022*
slope PK1-PK2 compared to PK2-PK3	*6.7e-16*	0.34	*0.00021*	*6.8e-9*	*3.4e-16*	0.05	0.32
slope PK3-PK4 compared to PK4-PK5	*4.7e-22*	*0.00075*	*3.7e-8*	*6.2e-19*	*2.0e-16*	0.77	0.10
Model Condition	**M-current mediated spiking beta (transient events)**	**M-current mediated spiking beta (continuous drive)**					
number of beta events	50	50					
peak beta frequency	24	22					
period (ms)	41.67	45.45					
PK3 duration (mean +/- SD)	39.7 +/- 7.08	46.0 +/- 6.32					
PK3 - PK2 and PK4 +	no	no					
Magnitude of PK3 compared to PK1 & PK5	N/A	N/A					
Magnitude of PK3 compared to PK2 & PK4	N/A	N/A					
slope PK1-PK2 compared to PK2-PK3	0.1	0.013					
slope PK3-PK4 compared to PK4-PK5	0.15	0.72					

Table S4: Statistical Analysis of Beta Event Waveform Features in Each Model Condition in Figures 4-7. Table depicts number of unfiltered high-power beta events analyzed in each model condition, the corresponding beta frequency, the duration of the beta events and corresponding average number of periods in an event, the duration of the PK3 peak (time from PK2-PK4), evaluation of polarity of peak events, and p-values using one-way ANOVA for peak amplitude comparisons (see Experimental Procedures section "Common Procedures to Identify, Align, and Quantify Beta Event Waveforms For All Data Sets:"). In the M-current mediated simulations, the PK3 peak was not significantly different from zero rendering statistical comparison to side peaks/troughs non-applicable (N/A). The peak beta frequency for each simulation was chosen as the frequency with the maximum power in the beta band pooled over all data. The fifty highest power beta events at that fixed frequency (determined from peaks in wavelet spectral power) were used for subsequent analysis and were such that PK3 duration varied for each event. Significance level p<0.01. Statistical significance was met in each comparison only with non-rhythmic drive or when pairing 10 Hz proximal drive with 10 Hz distal drive for distal SD = 15ms, 10 ms, and 5 ms (Figures 4, 5 and S3). Significant values are italicized.

Animal	**Anesth. Mouse 1 (LN1997)**	**Anesth.Mouse 2 (LN2182)**	**Awake Monkey 1 (Bertha)**	**Awake Monkey 2 (Pebbles)**	**Awake Monkey 3 (Winnie)**
number of beta events	50 (1 penetration)	100 (2 penetration)	650 (13 penetration)	200 (4 penetration)	600 (12 penetration)
peak beta frequency	18	18	15	18	20
period (ms)	55.56	55.56	66.67	55.56	50.0
number of periods in a beta epoch	2.95	3.17	3.52	2.54	3.19
PK3 duration (mean +/- SD)	60.9 +/- 10.6	51.4 +/- 11.2	53.4 +/- 5.82	45.0 +/- 5.82	43.4 +/- 7.22
PK3 + PK2 and PK4 -	yes	yes	yes	yes	yes
magnitude of PK3 compared to PK1 & PK5	*8.1e-48*	*2.4e-50*	*3.7e-165*	*1.1e-94*	*1.6e-91*
magnitude of PK3 compared to PK2 & PK4	*2.12e-37*	*2.1e-26*	*2.3e-62*	*2.7e-64*	*6.2e-53*
slope PK1-PK2 compared to PK2-PK3	*7.3e-24*	*6.5e-17*	*9.1e-36*	*4.5e-38*	*1.5e-30*
slope PK3-PK4 compared to PK4-PK5	*2.5e-15*	*2.1e-23*	*5.2e-37*	*4.63e-62*	*7.2e-37*

Table S5: Statistical Analysis of Beta Event Waveform in Granular Layer LFP in each Animal in Figure 8. Table depicts number of unfiltered high-power beta events analyzed in each condition, the corresponding beta frequency and period, the average number of periods in an event using a 98% power threshold determined from an empirical distribution of all beta activity, the duration of the PK3 peak, evaluation of polarity of peak events, and p-values using one-way ANOVA for peak amplitude comparisons (see Experimental Procedures section "Common Procedures to Identify, Align, and Quantify Beta Event Waveforms For All Data Sets"). Significance level p<0.01 (Bonferroni corrected for multiple comparisons across 5 animals p = 0.05/5). The peak beta frequency for each animal was chosen as the frequency with the maximum power in the beta band pooled over all data. The fifty highest power beta events at that fixed frequency (determined from peaks in wavelet spectral power) were used for subsequent analysis and were such that PK3 duration varied for each event. Statistical significance was met in each comparison for each animal considered, confirming that the features of the waveforms of the beta events in the granular layer LFP were consistent with the human data (Figure 8). Significant values are italicized.

Supplemental Figures

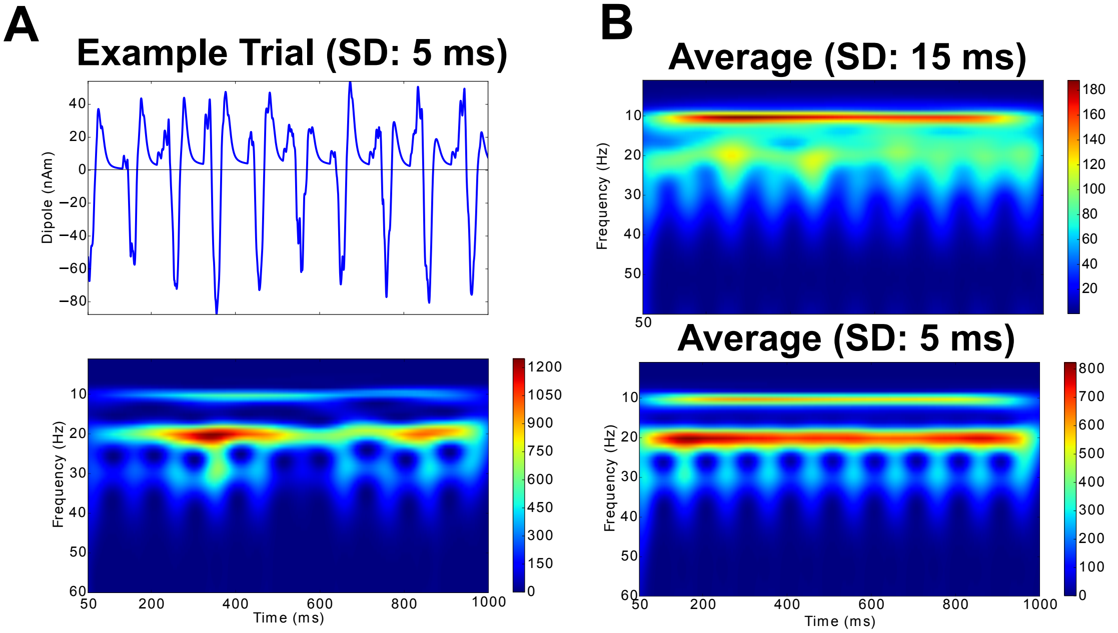

Figure S1: With Nearly-simultaneous 10 Hz Proximal and Distal Drives (as in Figure 5) the Relative Alpha to Beta Expression was Determined by the Standard Deviation (SD) of the Distal Drive. A. Example 1-second waveforms and time-frequency spectrogram from nearly-simultaneous 10 Hz proximal and distal drive (top panel) where the SD of the distal drive spikes on each cycle of the input was decreased to 5 ms (proximal drive SD 20 ms). As compared to a distal SD of 15 ms (Figure 5), beta activity becomes more prominent. In this case, it was also possible to have multiple prominent beta events in a row lasting > 3 cycles, however such activity was rarely seen in our MEG data (Table S1 and S2). **B.** Average of 100 1-second simulations with a SD of 15 ms (top) or 5 ms (bottom) shows that the relative alpha to beta expression changes. Alpha is prominent from larger distal SD, and beta is prominent for smaller distal SD, see also Figure 8 in Jones et al. J. Neurophys. 2009. Spectrogram units $(Am)^2$.

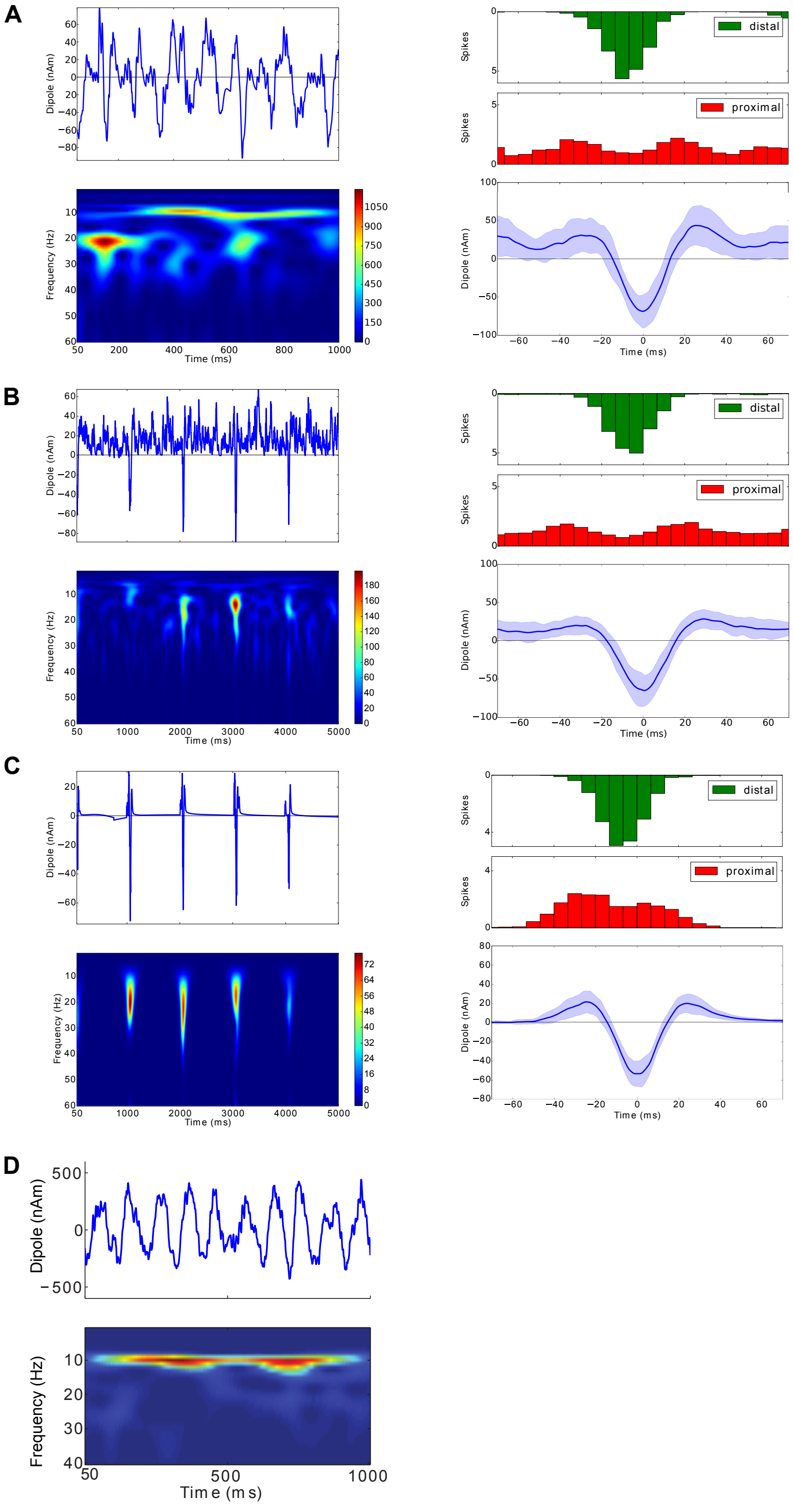

Figure S2. Additional Model Results Relevant to Figure 5 with Variation of Parameters of Proximal and Distal Drive A. Left panels: Example current source waveform and corresponding spectrogram from uniform random proximal drive and 10 Hz distal drive (SD = 10 ms) over 1 second simulation. Right panels: Histogram of proximal and distal drive spike distribution during 50 high power beta events simulated this way, and average and SD of the beta event waveform during the high power beta events. As in Figure 4 and 5, beta events consistent with the human data occurred on cycles where there is a broad proximal drive disrupted by a simultaneous distal drive that lasted ~50 ms. **B.** Left panels: Example current source waveform and corresponding spectrogram from uniform random proximal distal drive and 1 Hz distal drive (SD = 10 ms) over a 5 second simulation. Right panels: Histogram of proximal and distal drive spike distribution during 50 high power beta events simulated this way, and average and SD of the beta event waveform during the high power beta events. Here again, beta events consistent with the human data occurred on cycles where there is a broad proximal drive disrupted by a simultaneous distal drive that lasted ~50 ms. **C** Left panels: Example current source waveform and corresponding spectrogram from simultaneous 1 Hz proximal drive (SD = 20 ms) and distal drive (SD =10 ms). Right panels: Histogram of proximal and distal drive spike distribution during 50 high power beta events simulated this way, and average and SD of the beta event waveform during the high power beta events. Again, beta events consistent with the human data occurred this time on every cycle where a broad proximal drive was disrupted by a simultaneous distal drive that lasted ~50 ms. Note that in panels A-C the rising endpoints and resultant PK1 and PK5 peaks of the average human beta event waveforms were missing, and emerged when the drives were simulated to be nearly simultaneous at 10 Hz (Figure 5). **D**. Example current source waveform and corresponding spectrogram from anti-phase 10 Hz proximal and distal (50 ms delay between inputs) generated a pure alpha oscillation, see Ziegler et al 2010. Spectrogram units $(Am)^2$.

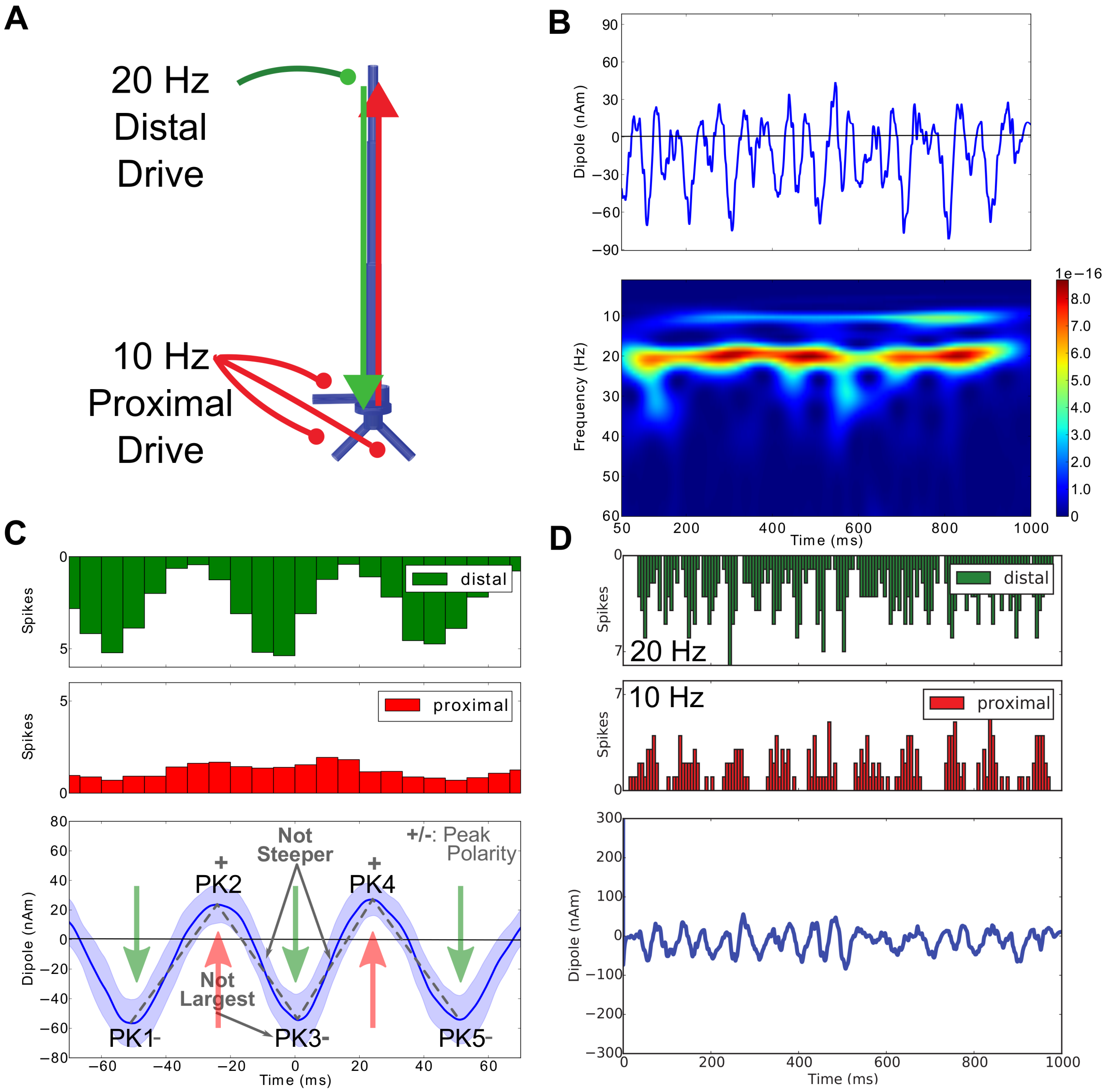

Figure S3. Additional Model Results Relevant to Figure 6 A. Simulation schematic with 20

Hz distal drive (10 ms SD. per cycle) and 10 Hz proximal drive (20 ms SD. per cycle) and mean delay between drives 0 ms. Other lags did not qualitatively change the results. **B**. This pairing also generated neocortical beta events. Alternating current flow was driven up and down the PN dendrites creating an oscillatory signal around zero, as in the human data. Spectrogram units $(Am)^2$. **C.** Once again, the beta event did not reproduce the statistically robust shape of our human data. The magnitude of the PK1 and PK5 troughs were statistically the same as PK3, and the sharp transitions around the PK3 trough relative to the neighboring peak transitions were again missing ($p>0.01$ all comparisons; Table S4), suggesting that this simulation cannot completely account for all the features of our recordings. **D.** Corresponding 1-second driving spike histogram and current dipole waveform. Please see additional discussion relevant this simulation below in Supplemental Discussion section "*Differences in Beta Events in SI and IFC and Other Possible Mechanisms of Beta Generation".*

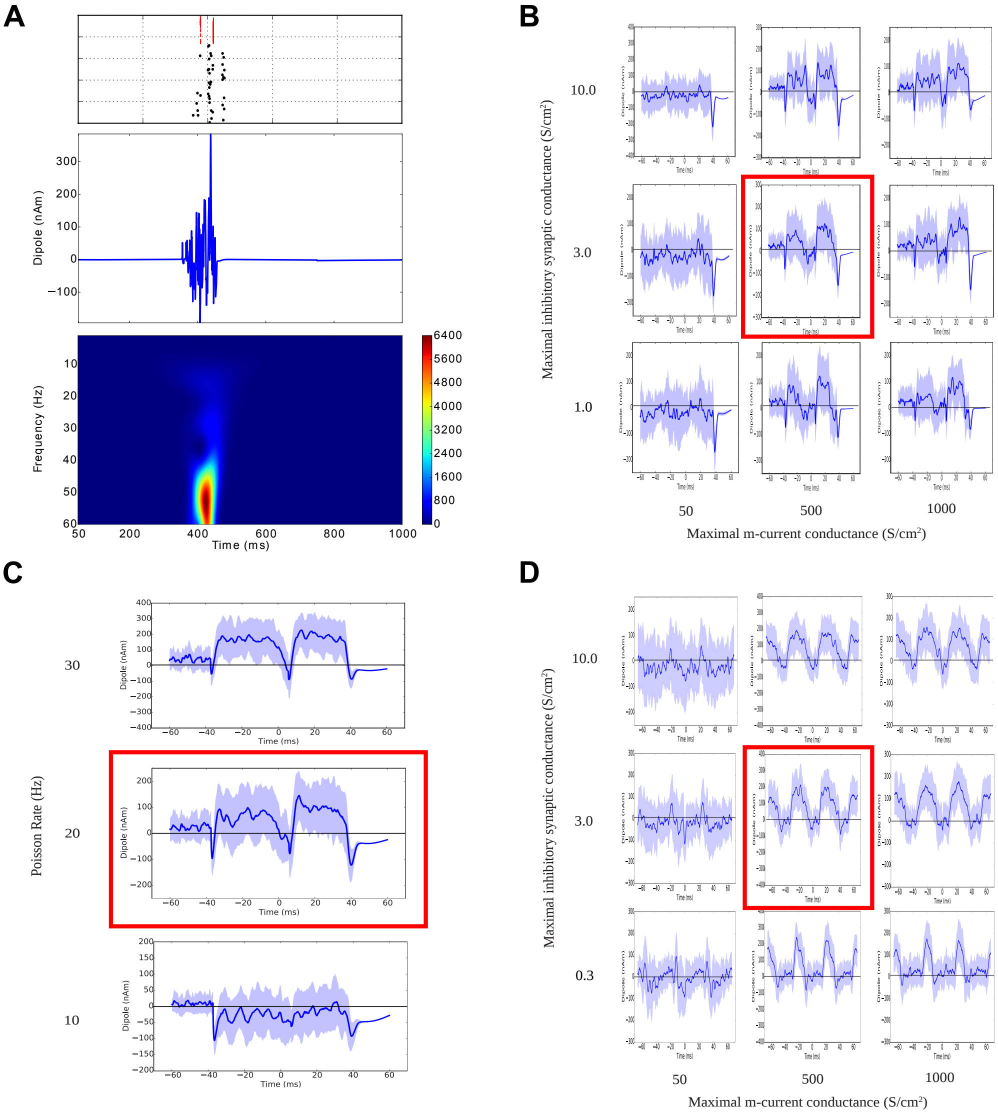

Figure S4 Additional Model Results Relevant to Figure 7 with Variation in Local Inhibitory Synaptic Conductance, M-Current Conductance and Noisy Poisson Drive

A. Example non-averaged simulated transient beta event showing spiking activity in inhibitory (red) and pyramidal neurons (black) (top panel), and corresponding current source waveform (middle panel) and spectrogram (bottom panel; units $(Am)^2$) induced by a brief bout of noisy drive to the pyramidal neurons in the default parameter regime as in Figure 7B, except that the duration of the noisy drive was reduced from 150 ms to 100 ms. In this case, beta events do not emerge on single trials because the E-cells are less synchronized and the noisy input dominates the current dipole signals. **B.** Average and SD of 50 high power transient beta events simulated exactly as in Figure 7B with varying levels of inhibitory and M-current conductance. Despite 3 fold changes in parameter values the PK3 trough does not become the dominant defining feature in the beta event waveforms and the side troughs remain roughly the same magnitude. **C.** Average and SD of 50 high power transient beta events simulated as in the middle box in panel B for 3 levels of transient noisy Poisson drive to the PN neurons. **D.** Average and SD of 50 high power beta events during continuous Poisson drive to PN as in Figure 7D-E for varying levels of local inhibitory synaptic conductance and M-current conductance. In each panel, red boxes denote default parameter regime as in Figure 7 and used for statistical analyses in Table S4 (see Supplementary Experimental Procedures Computational Neural Modeling Section "M-current mediated rhythms" for parameter values).

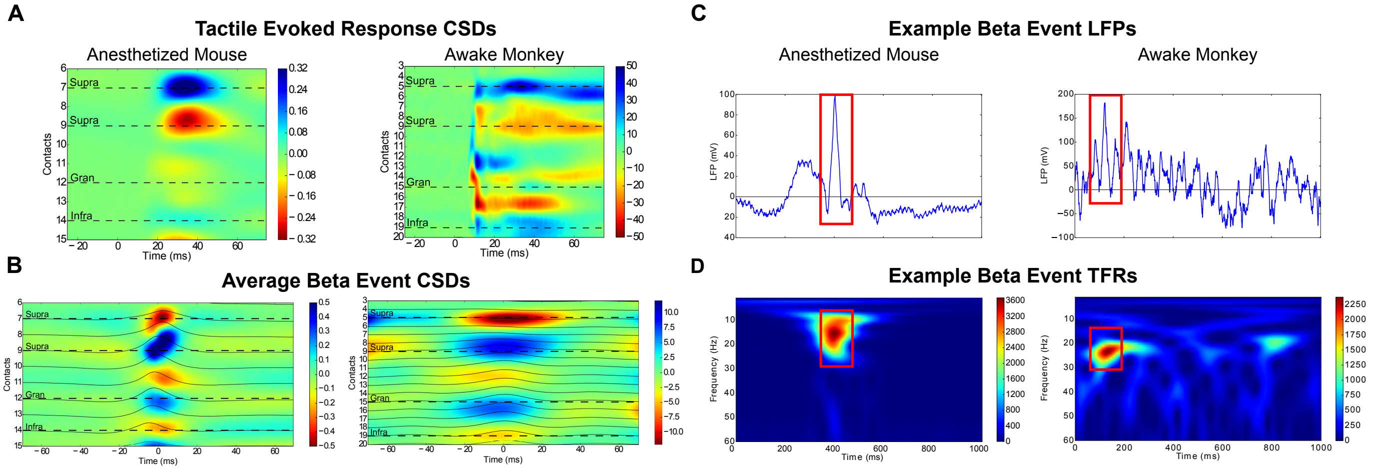

Figure S5. Additional Laminar Data Relevant to Figure 8 A. Example of tactile evoked responses to define layers in anesthetized mice (average n = 500 airpuff stimuli to vibrissa 3 second ISI as in (1)) and awake monkeys (average n = 227 contralateral median nerve stimulation 625 ms ISI as in (2)). Examples are as shown in Figure 8B-C. **B.** Example CSD pattern from laminar recordings in an anesthetized mouse and awake monkey SI during high power beta events. Examples shown are as shown in Figure 8B-C. Overlaid in black are aligned LFP beta event waveforms from each recording electrode. High power beta events were defined by the granular layer channel (layer IV), however similar attenuated waveforms existed in other channels emphasizing the dominant impact of the supragranular sink activity in inducing intracellular currents in the apical dendrites of the infragranular layer pyramidal neurons that created the extracellular LFP signal in cortex (Figure 2). **C-D.** Example granular layer LFP and corresponding time-frequency spectrogram over 1-second of spontaneous data in an anesthetized mouse and awake monkey show transient high-power beta events analogous to the human MEG data (see Figure 1 and also (3)). In each data set, LFP signals were referenced to a skull screw. Spectrogram units $(Am)^2$.

Supplemental Discussion

Relationship Between Co-occurring Alpha and Beta Activity

In SI, beta events are often co-expressed with 7-14 Hz alpha events, and in averaged spectrograms look coincident (4). Such co-occurrences are commonly referred to as mu-rhythms. Historically, the term "mu" refers to rhythms measured with EEG over Rolandic neocortex and are often dominated by alpha activity (e.g. (5)). We have shown that in IFC beta activity can also be co-expressed with alpha. In either area, the two rhythms are not inherently obligated to be expressed co-dependently and their relative activity is trial and subject dependent (e.g. Figure 1). We have previously shown that while high power in one band predicts high power in the other above chance, they are not obligated to co-occur in SI (please see (4) for an extensive review). Power spectral density plots from individual subjects had independent and varied peaks in each band showing they are separable across individuals (Figure 3 in (4)). Our prior studies have also shown that the power of the beta component of the SI mu rhythm increased with healthy adult aging, while alpha power did not, and our model showed that increased synchrony in the distal drive could explain the relative beta increase with age (6). Several other studies have suggested independence of alpha and beta. Alpha and beta activity in SI and IFC were coordinated during cued attention tasks, such that averaged power and synchrony increase in each band during inattention (4, 7). However, the spatial and temporal distribution of these effects were disjoint. During tactile detection tasks, beta was a better predictor of failed detection than alpha (8). These prior studies suggested a functional separation of the alpha and beta components, and our modeling has provided a mechanistic explanation as to how the relative expression can vary.

Relationship to Disrupt Beta in Parkinson's Disease

We have conjectured that the VM nucleus of the thalamus could provide the distally projecting input required to produce beta. The VM are known to be under inhibitory drive from the basal ganglia, rendering it particularly prone to 10 Hz rhythmicity that integrates to beta events in our model, since thalamic nuclei are known to generate 10 Hz rebound bursting when inhibited (9, 10). This prediction directly connects our theory to the origin of beta disruption in PD (10-13). Beta rhythms are known to be hyper-synchronous within and between basal-ganglia and motor circuits in PD patients (13). Despite such synchrony, a recent study has shown that the amplitude of resting-state beta rhythms in motor neocortex are decreased in PD compared to healthy controls (12). We postulate based on our model that the increased basal-ganglia to thalamus inhibition, known to exist in PD patients, might create a more diffuse and less focal inhibition of thalamus replacing localized burst synchrony with diffuse activation. In turn, this could decrease beta amplitudes in focal motor cortical signals, since the input to cortex would be less synchronous and thus effectively weaker, while preserving hyper-synchrony among basal ganglia and motor circuits.

Relationship Between Beta Generating Mechanisms and Known Circuit Biophysics

Our new mechanism for beta generation require that the distal excitatory synaptic drive is effectively stronger and faster than the proximal drive. Stronger distal and weaker proximal inputs seems counter intuitive to the well-documented fact that intrinsic and synaptic time-constants increase away from the soma up apical dendrites (i.e., distal responses are slower and attenuated) (14). Consistent with these biophysical facts, the geometric and intrinsic cellular properties of our model PNs reproduced an attenuated and slower response to excitatory synaptic input to the distal dendrites as compared to the proximal dendrites when only a single synapse of the same strength drive was simulated (Figure S6). Our results showed that a strong enough distal driving input can override these intrinsic cellular properties and produce a strong downward deflecting dipole current creating the prominent peak in the beta event waveform. A strong distal drive could be created by decreasing the variance of the driving spike pattern (e.g. increasing the synchrony) or increasing the post-synaptic conductance. A strong distal excitatory synaptic current during beta events was supported by our laminar recordings (Figure 9) and is in agreement with the idea that the supragranular layers of neocortex are densely innervated by both cortical-cortical synaptic connections and wide spread thalamic cortical connections (15, 16). While the functional significance of the simultaneous proximal and distal excitatory drive predicted by our model are unknown, the initial longer lasting proximal drive could also act as an amplifier to the subsequent distal input by providing an initial depolarization of the distal dendrites.

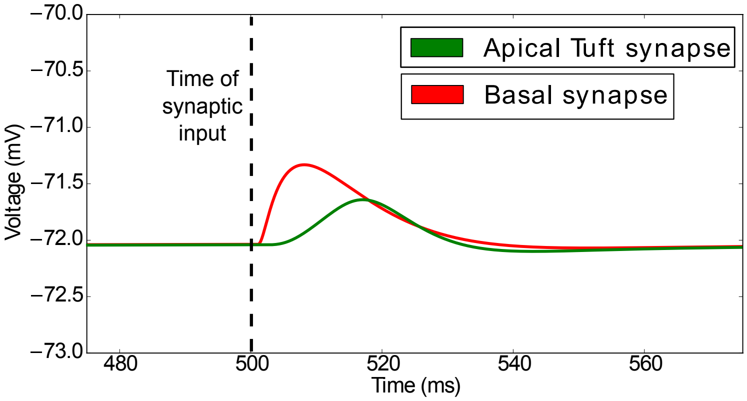

Figure S6. Somatic voltage responses in single PN to individual synaptic inputs at apical tuft (top compartment) or basal synapse (bottom compartment) showed distal inputs were slower and attenuated as compared to proximal inputs due to morphology and intrinsic cellular properties, consistent with known neocortical PN biophysics.

Differences in Beta Events in SI and IFC and Other Possible Mechanisms of Beta Generation

While the dominant features defining beta events were consistent in SI and IFC, there were some differences in the averaged beta event waveforms in these areas. The beta events in IFC tended to be faster than the beta events in SI and had more prominent negative PK1 and PK5 troughs. We explored how these differences could be reproduced in the model and found that changing parameters of the distal input were sufficient. As described in the results, an amplitude modulated 20 Hz distal excitatory drive (creating PK1, PK3 and PK5) paired with a simultaneous broad proximal input (creating PK2 and PK4) could reproduce the average IFC beta event waveform particularly well, as could a strong 10 Hz distal drive with larger variance (Figure 5C blue trace). Our laminar recordings from SI do not show evidence of a 20 Hz excitatory distal drive during the beta events (Figure 9), however we cannot rule out this possibility in IFC. Prior studies have suggested a direct connection between supplementary motor neocortex and IFC could mediate beta frequency coordination between the two areas during response inhibition (17), but such coordination could also be mediated indirectly through thalamic inputs to prefrontal neocortex (18).

Despite subtle differences, the main feature defining the beta events in both SI and IFC was a sharp negative PK3 trough flanked by smaller positive PK2 and PK4 peaks, which formed an inverted Ricker-wavelet shape. Reproduction of these features in our model required a flip in axial current flow within the PN dendrites, such that currents go weakly up then strongly down then weakly up the long apical dendrites (creating PK2, PK3, PK4, respectively). This pattern was reproduced with competing weak proximal and strong distal subthreshold excitatory synaptic inputs in our model and supported by laminar non-human recordings in SI. We tested several other mechanisms of beta generation that did not reproduce this pattern of current flow. However, we cannot rule out other patterns of drive that might also create this sequence in the current source signal. For example, subthreshold distal input composed of weak inhibitory synaptic drive, followed by strong excitatory drive, followed again by weak inhibitory drive, could induce the required flip in axial currents. A similar pattern of subthreshold proximal input composed of weak excitation followed by strong inhibition, followed again by weak excitation, might also work. That said, we note that even strong inhibition at the soma does not produce large downward deflecting current source signals, rendering this possibility unlikely (Figure S4).

A main reason that 20 Hz distal drive was insufficient to reproduce the statistically robust shape of the human beta event in both Figure 6 and Figure S3 was that the drive on either side of the central trough (PK3) was effectively too strong, so the side troughs (PK1 and PK5) were comparable in magnitude and sharpness to the PK3, creating a sinusoidal shaped waveform (Figure S3). These side troughs (PK1 and PK5) can be reduced by decreasing the frequency of the excitatory distal drive to 10 Hz (Figure 5D). They can also be reduced by simulating 20 Hz distal drive that comes in weak, then strong, then symmetrically weak (inducing PK1, PK3 and PK5 peaks), paired with simultaneous broad proximal drive (inducing PK2 and PK4 peaks). To our knowledge, there is no evidence of exogenous thalamic or higher order cortical activity that might provide this specific pattern of distal input.

Lastly, our laminar SI current source density recordings are in agreement with our model predictions, and not the many other possibilities described above. These data show a strong distal excitatory synaptic event lasting ~50 ms at the time of the PK3 activity in the beta events (Figure 9), albeit weak inhibitory inputs in distal layers could be masked by this strong excitatory drive.

Supplementary Text Describing Experimental Procedures

MEG Data Collection

General Procedures: All MEG data was collected with informed consent. MEG neuromagnetic responses were recorded with 306 sensors arranged in triplets of two planar gradiometers and a magnetometer at 102 sites (Elekta- Neuromag Vectorview). The data were sampled at 600 Hz.

SI data: MEG data were collected from 10 neurologically healthy, right-handed 18-45-yr-old adults during a tactile detection task, as detailed in (4, 19). An equivalent current dipole source localization procedure was used to locate the primary current dipole source to contralateral SI using a signal-space projection method based on a two-dipole model (20, 21). This method projected the dominant activity from a brief suprathreshold tap to right index finger onto two dipoles, one in contralateral SI and one in contralateral SII. The contribution from SII was removed from the data and only the data from the SI dipole was considered (4, 19). Projection of the location of the SI dipole onto individual subject's MRIs confirmed that this source was localized to the hand area of SI, area 3b (4, 19). All SI data came from the forward solution from the SI source, which encompassed a larger cortical volume than the IFC signal described below. Here, zero polarity was defined during the inverse solution analysis as the magnitude at which the net electrical current dipole moment switches sign: Baseline subtraction or spectral filtering were not applied. In this experiment, onset of the tactile detection trial (details in supplemental text) was indicated by an auditory cue delivered to both ears for 2 s. During the auditory cue, a 10-ms finger-tap stimulus was delivered between 500 and 1,500 ms. Following the cessation of the auditory cue, subjects reported detection or non-detection. The auditory cue ended 1,000 ms before the next trial began. Spontaneous oscillations and high power beta events analyzed were taken from the 1,000 ms intervals preceding non-perceived threshold-level stimuli because such intervals exhibited higher levels of pre-stimulus beta power (8). We analyzed data from 100 such trials per subject.

IFC data: MEG data were collected from 9 neurologically healthy, right-handed adults during a cued-attention tactile detection task, as described in (7). In contrast to the localization method for SI described above, data were localized using a minimum-norm-estimate (MNE) inverse solution technique (22). Data were projected on several cortical regions defined on individual structural MRI images according to Destrieux cortical atlas parcellations, including two sub-regions of rIFC, the inferior frontal sulcus and the inferior frontal junction. Here, we considered data from the inferior frontal junction region as this region displayed strong beta frequency power and phase locking with SI (7). Forward solutions from this region of interest were averaged accounting for reversal of direction of current flow across sulci. With this method, the rIFC subregion studied represented a smaller cortical volume than that representing the SI data described above. As such, the magnitude of the unfiltered IFC current source signal is on the order of 100 times smaller and significantly noisier than in SI.

In this experiment, trials began with a visual cue instructing subjects to direct attention to either the left hand, left foot, or either. At least 1000 ms after the visual cue, a threshold-level tactile stimulus was delivered either to the left hand (third digit) or left foot (first digit). Following the delivery of the stimulus, subjects reported detection or non-detection of tactile stimulation in the attended location via a right-hand button press (subjects were cued for a response when the visual cue changed to a fixation cross at least 400 ms after the delivery of the stimulus). Spontaneous non-time locked oscillations and high power beta events were analyzed from the [-1,000, 0] ms pre-stimulus intervals before a tactile stimulus was delivered. Data presented were from conditions in which the subject was cued to attend to the foot because these trials tended to exhibited higher levels of pre-stimulus beta power (7). We analyzed data from 100 such trials per subject.

Computational Neural Modeling

Calculation of Primary Current Source: The SI primary current source (equivalent current dipole) was calculated as the net weighted sum of the intracellular currents flowing within the dendrites of the entire population of model Pyramidal Neurons in a direction perpendicular to the longitudinal axis of the apical dendrite (4, 23, 24). The current in each compartment was weighted by the length of that compartment. A scaling factor of 60,000 was multiplied by all simulated results to match the amplitude of the empirical data as described previously (4).

Defining trials: A trial refers to a single execution of the model with a defined set of simulation parameters. For a given set of parameter values, results varied across trials due to the stochastic nature of the exogenous proximal and distal drives (described in supplemental text below). For each set of parameters described in Figure 5-7 (Table S4) 50 trials were simulated for a duration of 1000 ms each, and the highest-power beta events was chosen from each simulation (see description of beta events below).

Single-cell morphology and physiology: Inhibitory interneurons (IN) in each layer were simulated as single compartments containing fast sodium (I_{NA}), fast potassium (I_{kdr}) and leak (I_L) currents to create spiking activity. Pyramidal Neurons (PN) in layer II/III and V were modeled based on the reduction by Bush & Sejnowski (25) and contained eight and nine compartments respectively. The PN in layer II/III contained I_{NA}, I_{kdr}, I_L, and an adapting potassium current (I_M) and produced an adapting spike train in response to somatically injected current. The layer V PN included the same currents as those in layer II/III PNs but with the addition of a calcium current (I_{ca}), a potassium-activated calcium current (I_{KCa}), and h- and T- currents in the somatic and dendritic compartments. The pyramidal neurons in our model included active conductances, however, at subthreshold activation levels these currents minimally influence the dendrite current flow. Rather, subthreshold current flow is determined by the time constants of synaptic activation and the cable properties of the dendrites. In all simulations, these features were held constant.

Local Network Connectivity: Our simulated SI cortical column consisted of neurons in layers II/III and V with 100 pyramidal neurons (PN) and 35 inhibitory neurons (IN) per layer. Intra-columnar synaptic connections were modeled as depicted in Figure 3A. Synapses were representative of axonal-to-dendritic connections; however axons were not explicitly modeled. PN were arranged in a two-dimensional grid as shown in Figure 3D. INs were interleaved between every two PNs. Fast and slow excitatory (α-amino-3-hydroxy-5-methyl-4-isoxazolepropionic acid/N-methyl-D-aspartate [AMPA/ NMDA]) and inhibitory (γ-aminobutyric acid type A/type B [GABAA /GABAB]) synapses were simulated using an alpha function that became active when the soma of the presynaptic cell rose above 0 mV. The synaptic dynamics were defined by the following rise/decay time constants and reversal potentials, respectively: AMPA 0.5/5 ms, 0 mV; NMDA 1/20 ms, 0 mV; GABAA 0.5/5 ms, -80 mV; GABAB1/20 ms, -80 mV. The conductances of the synaptic connections within the local network grid were defined with a symmetric 2D Gaussian spatial profile, with a delay incorporated into the synaptic connection between two cells defined by an inverse Gaussian. In all simulations, these features where held constant, and during subthreshold drive to the local network these synapses remained inactive.

M-Current Mediated Rhythms: In vitro slice recordings and modeling studies have demonstrated that M-current gated beta oscillations can emerge from spike-mediated interactions within local neocortical networks (26, 27). Other factors contributing to beta generation in slice include gap-junction connectivity among pyramidal neurons and time constants of local inhibition, depending on the preparation (26). To simulate such M-current mediated rhythms (Figure 7, Figure S4), we used a reduced representation of our cortical column model. These simulations employed only layer II/III and the network was constructed as in our prior publication (28) which details the emergence of MEG rhythms generated by spike mediated synaptic interactions of PNs and INs. Transient beta oscillations were simulated by briefly driving the PN in the network with a noisy synaptic drive and the INs with an applied current. Continuous beta oscillations were simulated similarly but with Poisson drive to the PNs and an applied current to the INs for 1-second. The default values that created the beta frequency activity as in Figure 7 were as follows. Transient beta events: local inhibitory connections gmax = 3.0 mS/cm^{2,}, M-current conductance in PN 500 mS/cm^2, and rate of Poisson drive to PNs 20 Hz with gmax 0.01 mS/cm^2 and duration 150 ms: Applied current to the INs 0.25 mA, duration 75 ms beginning 25 ms after the start of Poisson drive to the PNs to enable the first bout of PN firing. Continuous beta events: same as transient drive case except the Poisson input to the PN and a tonic level of injected current to IN was present the entire simulation. Parameter adjustments around these default values are labeled in Figure S4.

Proximal and Distal Drive: Exogenous proximal and distal excitatory synaptic drives were simulated with connectivity profiles as in Figure 3B-C. In accordance with literature on lemniscal thalamic input, the proximal drive was modeled as propagating directly from layer IV to the basal and transverse dendrites of layer II/III and layer V PNs. The distal input representative of non-lemniscal pallidal thalamic drive contacted the apical dendrite of layer II/III and layer V PNs. To account for the greater number of proximal synaptic contact sites (3 proximal contacts, 1 distal contact), the maximal conductance of the distal synapses were set to be twice as strong as the maximal conductance of the proximal synapses. All conductance were chosen so the response remained subthreshold (29). The maximal conductances of each of the proximal and distal inputs to the PNs were 0.2 pico Siemens (pS) and 0.4 pS, respectively, and to INs were 0.4 pS and 0.8 pS, respectively. The exogenous driving input were each simulated with 10 pairs of spikes with an interspike interval of 10 ms (9) that activated glutametergic AMPA synapses. The cortical arrival time for each pair of spikes was drawn from a Gaussian random distribution around a mean arrival time and with variance as describe in text.

Each exogenous drive was modeled as rhythmic where each cycle consisted of "bursts" of input composed of 10 pairs of spikes with a mean interspike interval of 10 ms within the pair (9). As before (4), the mean arrival time for each pair of spikes was drawn randomly from a Gaussian random distribution with a predefined standard deviation (e.g. 5, 10, 15, or 20 ms, as in Table S4) and mean calculated as follows. The number of bursts per 1-second simulation was defined by the frequency of the input where the mean time between each cycle was the period of the chosen frequency of drive (e.g. 20 Hz or 10 Hz as in Table S4). The mean of the first burst was 50 ms into the simulation and the mean of each subsequent cycle was taken as the mean of the previous cycle increased by the period of the chosen frequency. This mean was used as the mean for the Gaussian distribution of each burst. Given the stochastic nature of the bursts, the net postsynaptic conductance of the proximal and distal drives varied on every cycle of input. The mean delay between the arrival of the proximal and distal input was set to 0 ms for all simulations.

Simulation parameters A fixed time-step implicit Crank-Nicholson solver was employed with a time increment of dt = 0.025 ms. In this publication, the code was adapted from our prior studies to run using the python programming language with the NEURON package and updated for parallel processing.

Animal Data

Extracellular Laminar Recordings in Anesthetized Mice

General Procedures: Local field potential (LFP) laminar recording data were obtained across the SI vibrissa barrel neocortex in two neurologically healthy, anesthetized mice (one recording session for Mouse 1; two recording sessions for Mouse 2) using NeuroNexus Probes. LFP Signals were sampled, filtered, and recorded using a Cheetah Data Acquisition System (NeuraLynx). A recording session was characterized by a new penetration of SI with the laminar probe. The probe was lowered to 1,600 um into SI. Response to vibrissa deflections were used to confirm placement. Ten minutes of baseline activity was recorded before a stimulus period consisting of 500 vibrissa deflections. This was followed by an additional ten minutes of post-stimulus recording. For the purpose of this study, high power beta events (Figure 8) were analyzed only in the 10-minute baseline recording period. Beta events in this baseline period were determined and sorted by power as described below and the top 50 power events in each penetration were used for subsequent analyses. Vibrissa stimulation data was used to determine neocortical layers, as described below. The surgical and recording methods were as described previously (1) and summarized below.

Surgical Procedures: Animals were anesthetized with 3.0% isoflurane in O_2 within an induction chamber fitted into a stereotaxic apparatus. Throughout the surgery, animals received 0.5-2.0% isoflurane in 1.0% O_2. Additionally, animals received 0.05 mL intraperitoneal injections of atropine sulfate, buprenorphine hydrochloride, and 0.025 of dexamethasone. Body heat was maintained at 36-38^{o}C with a heating pad both during surgery and recording session. The dorsal surface of the head was shaved with a standard razor, and any residual fur was removed using a depilatory agent. Skull was exposed under aseptic conditions, and the center of the planned craniotomy was marked. A custom-designed titanium head-post was affixed to the skull perpendicular to the sagittal plane. Dental cement was used to form a surface within the head-post interior for a saline well. The tissue surrounding the head-post was reattached to the head-post exterior edge using superglue. A pneumatic drill outfitted with a 0.5 mm regular carbide bur was used to clean away cement at the craniotomy site and thin the skull. The bone was removed, and the exposed brain was covered with saline. Following recordings, the saline well was filled with a silicone elastomer to cap and protect the craniotomy. At the start of subsequent recording sessions, the silicone was removed and the surgical area inspected for bleeding, inflammation, and bone growth. Recordings then proceeded as described below.

Laminar Data Acquisition: All recording equipment was secured onto a vibration isolation table to minimize noise and artifact. Animals were head-fixed, and anesthesia was maintained through infusion of 0.5-2.0% isoflurane through a nose cone; isoflurane levels were gradually lowered until the animal was just above the threshold at which there existed a paw pinch response.

NeuroNexus probes with 16 contacts spaced 100 µm apart was lowered at a controlled rate until the bottom contact was at a depth of 1600 µm using a four-point axis micromanipulator. The probe was grounded on the head-post mount, and a reference wire was placed in the saline well. An air puffer controlled by a solenoid was positioned above the contralateral vibrissae and used to test for response to vibrissa deflection to confirm proper electrode placement in SI and to assign neocortical layer position to each probe contact (see below).

After confirmation of electrode placement, recording began. LFP signals were sampled at 30303 Hz using a Cheetah Data Acquisition System and subsequently filtered to 1010.10 Hz prior to analysis. Recording sessions began with 10 minutes of baseline activity recording. Following this was a stimulus period consisting of 500 air puff trials delivered to the contralateral primary vibrissae. Inter-trial periods were randomly selected to be between 2 and 8 seconds in duration with mean period of 5 seconds. For the purpose of this study, high power beta events (Figure 8 and 9) were analyzed only in the 10 minute baseline recording period. Beta events in this baseline period were determined and sorted by power as described below and the top 50 power events in each penetration were used for subsequent analyses. Air puff stimulation data was used to determine neocortical layers, as described below.

Extracellular Laminar Recordings in Awake Monkeys

Surgical Procedures: Animals were surgically prepared for chronic awake electrophysiological recording using standard methods (30). Preparatory surgery was performed under deep (1–3%) isoflurane anesthesia. A titanium head post was fastened to the posterior skull using titanium orthopedic brackets and bone screws to allow painless restraint of the head during recording.

Plastic recording chambers were positioned bilaterally over craniotomies exposing the region of the primary cortical hand representation at the lateral portion of the central sulcus. Each recording chamber was positioned to optimize the angle of penetration in area 3b to the greatest extent possible and entailed orienting the chambers so that initial cortical penetration occurred at an angle of 60°, depending on the anatomy of each hemisphere in each animal. Care was taken to maintain the dura intact.

Median Nerve Stimulation: After recovery from surgery, monkeys were accustomed to a primate chair and head restraint. They were not required to attend to or discriminate any of the stimuli, but rather, were explicitly habituated to electrical median nerve stimulation. Two gold cup electrodes were positioned over the median nerve just proximal to the wrist and electrical stimulation from a GRASS S8 stimulator (Astro-Med) delivered a 200-μs duration square-wave pulse at 0.5 Hz. Stimulus intensity was titrated before each session to just subthreshold for the adductor pollicis brevis (APB) twitch. Stimulus intensity was monitored continuously (using the distal APB twitch) during recording. Recorded median nerve responses in the contralateral hemisphere were used to confirm electrode placement in area 3b of SI and to identify neocortical layer positions for each probe contact (see below).

Laminar Data Acquisition: Data were collected with a 0.34 mm-diameter laminar Neurotrak probe with 24 electrodes spaced 200 μm apart. Area 3b was targeted using several approaches including high-resolution presurgical magnetic resonance imaging (MRI), initial penetration mappings in posterior bank of central sulcus, and post-experiment histological confirmation of penetration location. A reference wire was placed epidurally over the contralateral sensorimotor cortex.

During collection, LFP data from each channel were amplified (x1000) and bandpass filtered (0.1 to 3,000 Hz). Each recording session consisted of recordings of spontaneous neural activity (average length 4 min) and stimulation of the contralateral median nerve (mean of 140 stimuli/session). LFP signals were sampled at 2000 Hz. For the purposes of this study, beta events were analyzed only in the spontaneous recordings during non-task periods. Median nerve stimulation data was used to identify the neocortical layers.

Common Procedures to Identify, Align, and Quantify Beta Event Waveforms For All Data Sets:

To assure data was comparable across modalities, the following procedures were applied in the same manner to the human MEG primary current dipole data from SI and IFC, primary current source dipoles from model simulations, and granular layer LFPs from mouse and monkey laminar recordings.

Spectral Analysis: Time frequency representations (TFRs) or spectrograms of the spontaneous data were calculated from 1 to 60 Hz by convolving the signals with a complex Morlet wavelet of the form $w(t, f_0) = A\exp(-t^2/2\sigma_t^2)\exp(2i\pi f_0 t)$, for each frequency of interest f_0, where $\sigma_t = m/2\pi f_0$, and i is the imaginary unit. The normalization factor was $A = 1/(\sigma_t\sqrt{2\pi})$ and the constant *m* defining the compromise between time and frequency resolution was 7. Time-frequency representations of power were calculated as the squared magnitude of the complex wavelet-transformed data.

Defining High-Power Beta Events:

Overview: Our goal was to quantify high power beta events that where clear upon visual inspection of the spectrogram, as in Figure 1. Our human data consisted of 100 trials of 1second prestimulus data from each subject, in both SI and IFC. For each trial, we found all the maxima in the beta frequency of interest (see below “Choosing beta frequency of interest”), and then chose the event with highest power, leaving us with n = 100 events per subject. We then sorted these events from low to high power and only analyzed the top 50 highest power events (e.g. top ½ of the identified beta events), as described in “Details of analysis” below. For the animal data, we considered continuous streams of spontaneous (non-task) periods (10 minutes per mouse, 4min per monkey), identified all local maximum at the beta frequency of interest, sorted all such events from low to high power, and then analyzed the top 50 highest power events, as described in “Details of analysis” below.

Details of Analysis: For each person, animal and model simulation, 50 high-power beta events were identified (as described in “Overview” above) and aligned using a procedure that: 1) identified the frequency in the beta band (15 – 29 Hz) with the highest total power spectral density in the raw time-series data; 2) identified maxima in the TFR for this frequency of interest (FOI); 3) localized the features in the raw waveform which produced these maxima by band-passing the raw time series at the frequency of interest and identifying extrema within the band-passed signal which occurred closest in time to the TFR maxima (see details in *Choosing Beta Frequency of Interest* below). Importantly, the extrema were chosen to allow for consistent interpretation in terms of current flow within pyramidal neuron dendrites. For the human SI and model current source data this corresponded to choosing negative polarity extrema, and for the animal LFP data to choosing positive polarity extrema. The inverse method used to localize the IFC data (described above) does not enable a direct interpretation of the alignment of current flow to pyramidal neuron dendrites. In the case, we chose largest positive value extrema and conjectured that this corresponded to current flow down the dendrites since the results were remarkable consistent with the SI data. 4) The raw, unfiltered time-series was then truncated around the times at which the extrema from (3) occurred. We note that a low pass filter at 60 Hz was first applied to the IFC data to remove high frequency noise in this smaller volume signal. Of these truncated events, the top 50 of highest beta power were used for further analysis. We provide further details of each step below.

Choosing Beta Frequency of Interest: TFRs of the spontaneous data were calculated as described above. The beta frequency of interest for further analysis was chosen by summing the TFR across time for all data, producing a power spectral density representation (PSD), and identifying the frequency in the 15-29 Hz range with the greatest total power in the PSD. Due to a strong 1/f effect present in the PSDs of the anesthetized mice, we limited our frequency search to 18-24 Hz, since this was the range of frequencies of interest found in the human MEG data (Table S1). Individualized frequencies of interest (FOI) in the beta band were determined for each human subject, model simulation, and mouse penetration (Tables S1, S4 and S5). The FOIs in each monkey were calculated as the average across multiple penetrations (Table S5; monkey 1: 15.38+/-0.84 Hz; monkey 2: 18.25+/-1.79 Hz; monkey 3: 20.25+/-1.79 Hz).

Aligning Peaks: We then identified all *maxima* in the TFR (i.e. peaks in TFR beta “hot spots”) at the FOI and saved the times of these *maxima*. To ensure that beta event waveforms were aligned consistently within and across recording modalities, we aligned according to the polarity of peaks in the unfiltered time series waveform as follows. We band-passed the raw time series data at the frequency of interest using a linear phase non-causal fir filter, with zero phase lag, of width 2 Hz. Within the filtered data, we identified the closest *extrema* of correct sign (positive or negative) to the times saved from the prior identification of beta peaks in the TFR analysis. We then truncated the raw, unfiltered time-series by 1.5 periods of the frequency of interest on either side of the times at which these *extrema* occurred. In the transient spiking network simulations (Figure 7B-C), the time of peak activities in the beta events was set by the time window of the Poisson drive, which was the same across trials (150 ms duration). The Poisson drive was strong and acted like a switch to turn the network on and off, akin to an applied current over a predefined window. While there was some jitter in the exact spike times on different trials, particularly in the PNs, the timing of IN spiking that defined the beta event was consistent across trials. The beta event period (and specifically PK3 trough) was set by the time constant of decay of the inhibition and M-current kinetics, as in prior studies. Since we were controlling the time window of the Poisson drive to be fixed across trials, the IN spikes times were consistent. Therefore, we did not need to align peaks across trials and data were averaged over a predefined time window within the duration of the Poisson drive. Of note, using the same aligning procedure as in the human and animal data, often aligned to the wrong peak and in a large number of trials the waveforms become flat after t = 10 ms creating an erroneous reduction in the PK4 peak in the average (**Figure S7, left**). In contrast, when aligning over a predefined time window based on the duration of the Poisson drive, as in Figure 7B-C and Figure S4A-C, the smoothed version of the data shows that the PK3 peaks were consistently aligned without erroneously reducing peaks (**Figure S7, right**). In the continuous spiking network case, (Figure 7D-E) trials were aligned and averaged as in the human and animal data.

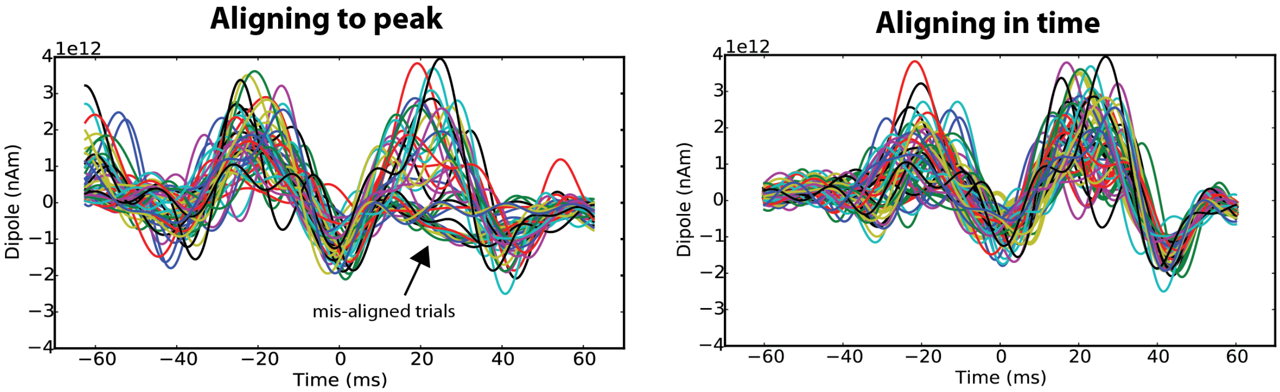

Figure S7. Illustration justifying the different aligning procedure for the transient spike mediated M-current simulations. (**Left**) Using the same aligning procedure as in the human and animal data, often aligned to the wrong peak and in a large number of trials the waveforms become flat after t = 10 ms creating an erroneous reduction in the PK4 peak in the average. In contrast, when aligning over a predefined time window based on the duration of the Poisson drive, as in Figure 7B-C and Figure S4A-C, the smoothed version of the data shows that the PK3 peaks were consistently aligned without erroneously reducing peaks. Note: Our peak finding procedure for waveform alignment was based on smoothed data (see SI Appendix, "Details of Analysis"). However, all aligned and averaged figures shown in the paper were based on unfiltered data.

A time vector for the stereotypical waveform from the unfiltered aligned data was constructed for each beta event such that the waveform was centered about t = 0 ms. In the human and animal data, we then sorted these beta events by their power and the top 50 highest power beta events were used for further analyses. All model data was obtained from 50 simulations with intrinsic noise determined by the simulation parameters.

Defining Duration of High-Power Beta Events: Our goal was to define a threshold to calculate duration that was below the peak of each of our 50 chosen high power beta events, and that considered only statistically significant beta power. Thus, to measure the duration of the 50 highest power beta events in each data set, we first constructed an empirical density function for the beta-generating process on a per-subject basis. For an individual subject or animal, the spectral power in each frequency in the beta-band (15-29 Hz) at every time point across every trial was pooled together, sorted across power, and binned into a histogram containing on the order of 1,000,000 data points. The histogram was normalized to integrate to one, thus creating an empirical density for each data set. The power of the 98th percentile was determined from the empirical densities, and thus contained statistically significant beta power ($p<0.02$). The duration of the beta events was then defined as the length of time during which the power of the beta event was above the corresponding 98th percentile power threshold. The beginning of an epoch was marked when the power in the beta band in the time-frequency spectrogram rose above this threshold, and the epoch ended when the power fell back below the threshold. The duration was simply calculated as the difference between the start and end times of an epoch. The 98th percentile was chosen as a cutoff as it was the most significant threshold, which was exceeded by at least all 50 high power beta events for every subject. In the human data the number of events above this cutoff was 113 +/- 48 in SI and 122 +/- 23 in IFC, and the percentage increase in maximum power of the beta events from the power this cutoff was 200 +/- 20% in SI, and 180 +/- 20% IFC. We note that due to smearing in the time domain that occurs with spectral analyses the duration of the beta event waveforms in the time-domain are likely slightly shorter than the spectrogram estimates in the supplemental tables.

Quantification of Beta Events: The definition of peak values used for statistical analyses described in all Supplemental Tables were as follows. For a given trial, the 50 aligned high-power beta event waveforms, described above, were convolved with a Hann window of length 10 * dt, where dt is the time step of the time series to smooth the signal. For each waveform, extrema were then identified and assigned labels, such that PK3 occurred closest to $t = 0$, PK2 and PK4, occurred immediately before and after PK3, respectively, and PK1 and PK5 occurred immediately before PK2 and after PK4, respectively. In one monkey not all peaks were present (see below). Magnitudes of the respective peaks were then assigned as absolute magnitude of the waveform occurring at these extrema times. The magnitude of PK3 was then compared to the magnitudes of PK2 / PK4 and PK1/PK5, respectively, by applying a one-way ANOVA to the 50 observations of each value to arrive at the magnitude comparison values given in Supplemental Tables SI, S2, S4 and S5. Slopes between peaks were calculated as the amplitude difference between the peaks divided by the time between the peaks. To test the hypothesis that the slope beteen PK2-PK3 was steeper (of larger absolute amplitude) than the slope between PK1-PK2, as in Tables S1, S2, S4 and S5, we took the absolute value of each slope and performed a one-sided T-test using the 50 observations of each measure. The same operation was used to test the hypothesis that the slope between PK3-PK4 was steeper than the slope between PK4-PK4. For MEG, model, and mouse signals, PK3 duration was calculated as the time between the PK2 and PK4 extrema due to the robust presence of these peaks on either side of PK3 (e.g. see main document Figure 1 Bi, Bii and 8B top panels for single event examples). In monkey signals, the PK2 and PK4 extrema were less robust (e.g. see main document figure 8C top panel for single event examples) and instead the PK3 duration was calculated as the time between the zero-crossings of the signal on either side of PK3. These two methods both produced durations near the beta period. We report the zero-crossing values in Table S5, due to the fact that there was less uncertainty (defined as SD/mean*100) in the zero-crossing duration calculation.

In one of the three monkeys (Awake monkey 1, Table S5), PK2 and PK4 could not be identified in 4 of the 13 penetrations, and PK1 and PK5 could not be identified in 9 penetrations. In these cases, PK2 and PK4 were chosen as the values at +/-55 ms, and PK1 and PK5 were chosen as the values at the endpoints of the waveform.

Features were labeled on all average beta waveform Figures as follows. PK3 was labeled as the “Larger” if its absolute magnitude was significantly larger than the absolute magnitude of PK2 and PK4 as determined by a one-way ANOVA, as in Tables S1, S2 and S4. The dashed lines connecting PK2 and PK4 to PK3 were labeled “Steeper” if the slopes of these line segments as calculated above were significantly larger in absolute magnitude than the slopes of the dashed lines connecting PK1 and PK5 to PK2 and PK4 respectively as determined by a one-sided T-test, as in Tables S1, S2 and S4. A peak was labeled with “+” if its magnitude was positive in sign and its standard error bounds did not overlap with zero; a peak was labeled with ‘-‘ its magnitude was negative in sign and its standard error bounds did not overlap with zero.

Correlation Between Beta Period and Peaks: The correlation between the width of a waveform feature (e.g. the width of PK3) and the beta period in Table S3 was determined as follows. For a given subject or model condition we had previously determined 50 high power beta events in the spectral transforms of the raw time-series signal as described above (“Defining High-Power Beta Events”). For each of these 50 high power events, we determined the frequency in the beta band (15-29 Hz) in which the highest power occurred. The period for that event was then taken as the inverse of that highest power frequency. We then calculated a Pearson’s correlation coefficient between the 50 measures of PK3 duration from the beta waveforms and the 50 high power frequencies for each subject or model condition. A similar analysis was performed between the PK1-PK2, and PK4-PK5 peaks, as defined above in *“Quantification of Beta Events”*.

Common Procedures For Current Source Density Analyses in Anesthetized Mice and Awake Monkey Data

Current Source Density Analysis: Current source density (CSD) profiles of laminar recordings were estimated and each probe contact was assigned to a neocortical layer. For the beta waveform analysis (described above) and beta event CSD analysis (described below), the LFP from a contact within the identified granular layer was used. However, waveforms in other contacts had similar temporal profiles (Figure S5B), suggesting the LFP beta event was generated by a highly synchronous process so that the LFP generator had a long spatial reach approximating that of a current dipole (31).

Current source density (CSD) profiles of laminar recordings were estimated using a three-point formula for the approximation of the second spatial derivative of voltage as a function of depth across channels, as in (32) and (33). The CSD was interpolated along the spatial axis using a bivariate spline approximation over a rectangular mesh in order to smooth and sharpen edges within the CSD.

Calculation of Beta Event CSD: For each animal, 50 high power beta events in the spontaneous signal from the granular layer were identified and aligned, as described above. For each of the 50 events, the corresponding LFP data from each contact was similarly aligned based on the granular layer beta event alignment. Data across the 50 events was then averaged for each contact and the CSD profile of the averaged data was considered the beta event CSD (Figure 9).

Neocortical Layer Assignment: The assignment of each probe contact to a specific neocortical layer was determined through examination of the average laminar LFP and CSD profiles evoked by all tactile stimuli from a recording session (either vibrissa deflection or median nerve stimulation for mouse and monkey, respectively. The border between granular and infragranular layers was defined by inversion of the LFP. Supragranular layers were assigned based on the presence of a strong sink/source pair in the superficial contacts (Figure S5A).

Quantification of Sink Activity in the Beta Event CSDs: To quantify the amplitude and duration of the sink activity in the supragranular layers (Figure 9), we found the sink of greatest absolute magnitude (i.e., the most negative) in the CSD from the supragranular channels in a restricted window around t = 0 ms (t = +/- 50 ms). The sink amplitude was calculated as the CSD magnitude at this *minimum*. An analogous procedure was applied to quantify the amplitude of the sink activity in the infragranular layers. To calculate the supragranular sink duration, a start/endpoint of the sink was defined either as the point at which the sink reached 15% of its maximum depth or as the point at which a local maximum was attained, whichever event occurred first. The time between the start and endpoint of the sink was defined as the sink duration. In the mouse data, the sink amplitude in the upper contacts was the same strength across multiple channels and the data was averaged across these channels.

Supplemental References

1. Normand EA*, et al.* (2013) Temporal and mosaic Tsc1 deletion in the developing thalamus disrupts thalamocortical circuitry, neural function, and behavior. *Neuron* 78(5):895-909.
2. Lipton ML*, et al.* (2010) Interactions within the hand representation in primary somatosensory cortex of primates. *The Journal of neuroscience : the official journal of the Society for Neuroscience* 30(47):15895-15903.
3. Feingold J, Gibson DJ, DePasquale B, & Graybiel AM (2015) Bursts of beta oscillation differentiate postperformance activity in the striatum and motor cortex of monkeys performing movement tasks. *Proceedings of the National Academy of Sciences of the United States of America* 112(44):13687-13692.
4. Jones SR*, et al.* (2009) Quantitative analysis and biophysically realistic neural modeling of the MEG mu rhythm: rhythmogenesis and modulation of sensory-evoked responses. *J Neurophysiol* 102(6):3554-3572.
5. Anderson KL & Ding M (2011) Attentional modulation of the somatosensory mu rhythm. *Neuroscience* 180:165-180.
6. Ziegler DA*, et al.* (2010) Transformations in oscillatory activity and evoked responses in primary somatosensory cortex in middle age: A combined computational neural modeling and MEG study. *NeuroImage* 52(3):897-912.
7. Sacchet MD*, et al.* (2015) Attention drives synchronization of alpha and beta rhythms between right inferior frontal and primary sensory neocortex. *J Neurosci* 35(5):2074-2082.
8. Jones SR*, et al.* (2010) Cued Spatial Attention Drives Functionally-Relevant Modulation of The Mu Rhythm in Primary Somatosensory Cortex. *Journal of Neuroscience* 30(41):13760-13765.
9. Hughes SW & Crunelli V (2005) Thalamic mechanisms of EEG alpha rhythms and their pathological implications. *Neuroscientist* 11(4):357-372.
10. Edgerton JR & Jaeger D (2014) Optogenetic activation of nigral inhibitory inputs to motor thalamus in the mouse reveals classic inhibition with little potential for rebound activation. *Frontiers in cellular neuroscience* 8:36.

11. Little S & Brown P (2014) The functional role of beta oscillations in Parkinson's disease. *Parkinsonism & related disorders* 20 Suppl 1:S44-48.
12. Heinrichs-Graham E*, et al.* (2014) Hypersynchrony despite pathologically reduced beta oscillations in patients with Parkinson's disease: a pharmaco-magnetoencephalography study. *J Neurophysiol* 112(7):1739-1747.
13. Brittain JS, Sharott A, & Brown P (2014) The highs and lows of beta activity in cortico-basal ganglia loops. *Eur J Neurosci* 39(11):1951-1959.
14. Stuart G & Spruston N (1998) Determinants of voltage attenuation in neocortical pyramidal neuron dendrites. *J Neurosci* 18(10):3501-3510.
15. Hutsler JJ, Lee DG, & Porter KK (2005) Comparative analysis of cortical layering and supragranular layer enlargement in rodent carnivore and primate species. *Brain Res* 1052(1):71-81.
16. Jones EG (2001) The thalamic matrix and thalamocortical synchrony. *Trends Neurosci* 24(10):595-601.
17. Swann NC*, et al.* (2012) Roles for the pre-supplementary motor area and the right inferior frontal gyrus in stopping action: electrophysiological responses and functional and structural connectivity. *NeuroImage* 59(3):2860-2870.
18. Barbas H, Garcia-Cabezas MA, & Zikopoulos B (2013) Frontal-thalamic circuits associated with language. *Brain Lang* 126(1):49-61.
19. Jones SR, Pritchett DL, Stufflebeam SM, Hamalainen M, & Moore CI (2007) Neural Correlates of Tactile Detection: A Combined MEG and Biophysically Based Computational Modeling Study. *Journal of Neuroscience* 27(40):10751-10764.
20. Tesche CD*, et al.* (1995) Signal-space projections of MEG data characterize both distributed and well-localized neuronal sources. *Electroencephalogr. Clin. Neurophysiol.* 95(3):189-200.
21. Uusitalo MA & Ilmoniemi RJ (1997) Signal-space projection method for separating MEG or EEG into components. *Med. Biol. Eng. Comput.* 35(2):135-140.
22. Gramfort A*, et al.* (2014) MNE software for processing MEG and EEG data. *NeuroImage* 86:446-460.
23. Murakami S & Okada Y (2006) Contributions of principal neocortical neurons to magnetoencephalography and electroencephalography signals. *J Physiol* 575(Pt 3):925-936.
24. Jones SR & Local Field Potential RtEEaMM (2014) Local Field Potential, Relationship to Electroencephalogram (EEG) and Magnetoencephalogram (MEG). *Encylopedia of Computational Neuroscience: SpringerReference*, ed Jaeger D. JR (Springer-Verlag Berlin Heidelberg).
25. Bush PC & Sejnowski TJ (1993) Reduced compartmental models of neocortical pyramidal cells. *Journal of neuroscience methods* 46(2):159-166.
26. Roopun AK*, et al.* (2006) A beta2-frequency (20-30 Hz) oscillation in nonsynaptic networks of somatosensory cortex. *Proceedings of the National Academy of Sciences of the United States of America* 103(42):15646-15650.
27. Yamawaki N, Stanford IM, Hall SD, & Woodhall GL (2008) Pharmacologically induced and stimulus evoked rhythmic neuronal oscillatory activity in the primary motor cortex in vitro. *Neuroscience* 151(2):386-395.
28. Lee S & Jones SR (2013) Distinguishing mechanisms of gamma frequency oscillations in human current source signals using a computational model of a laminar neocortical network. *Front Hum Neurosci* 7:869.
29. Zhu Z*, et al.* (2009) The relationship between magnetic and electrophysiological responses to complex tactile stimuli. *BMC neuroscience* 10:4.

30. Schroeder CE, Mehta AD, & Givre SJ (1998) A spatiotemporal profile of visual system activation revealed by current source density analysis in the awake macaque. *Cereb Cortex* 8(7):575-592.
31. Linden H*, et al.* (2011) Modeling the spatial reach of the LFP. *Neuron* 72(5):859-872.
32. Vaknin G, DiScenna PG, & Teyler TJ (1988) A method for calculating current source density (CSD) analysis without resorting to recording sites outside the sampling volume. *Journal of neuroscience methods* 24(2):131-135.
33. Schroeder CE*, et al.* (1995) Localization of ERP generators and identification of underlying neural processes. *Electroencephalography and clinical neurophysiology. Supplement* 44:55-75.